ASME Journal of Manufacturing Science and Engineering
Online journal at:
https://asmedigitalcollection.asme.org/manufacturingscience

Rayne Wolf
Mem. ASME
Department of Industrial
and Systems Engineering,
University of Wisconsin–Madison,
Madison, WI 53706
e-mail: rmwolf2@wisc.edu

Liangkui Jiang
Mem. ASME
Department of Industrial
and Systems Engineering,
University of Wisconsin–Madison
Madison, WI 53706
e-mail: ljiang248@wisc.edu

Khawlah Alharbi
Department of Industrial
and Systems Engineering,
University of Wisconsin–Madison,
Madison, WI 53706
e-mail: kaalharbi@wisc.edu

Pengyu Zhang
Department of Industrial
and Systems Engineering,
University of Wisconsin–Madison,
Madison, WI 53706
e-mail: pzhang256@wisc.edu

Chao Wang
Department of Industrial
and Systems Engineering,
University of Iowa,
Iowa City, IA 52242
e-mail: chao-wang-2@uiowa.edu

Hantang Qin[1]
Mem. ASME
Department of Industrial
and Systems Engineering,
University of Wisconsin–Madison,
Madison, WI 53706
e-mail: hqin52@wisc.edu

Heterogeneous Transfer Learning of Electrohydrodynamic Printing Under Zero-Gravity Toward In-Space Manufacturing

As we continue to commercialize space and mature in-space manufacturing (ISM) processes, there is a strong need to transfer the knowledge we learn from experiments on the ground to zero-gravity environments. Physics-motivated manufacturing processes, like additive manufacturing, experience a shift in fabrication parameters due to the absence of gravity and the change of environments. Thus, we found traditional machine learning methods are not capable of addressing this domain shift and present a transfer learning scheme as a solution in this paper. We tested a kernel ridge regression model built for heterogeneous transfer learning (KRR-HeITL) on data from the electrohydrodynamic inkjet printing (EHD printing) process. EHD printing is a process that uses electrical force to control material flows, thus achieving the fabrication of electronics without requiring gravity. Our team has successfully conducted three rounds of parabolic flights to validate this technology for ISM. We trained on multiple datasets built from on-ground experiments and tested using zero-gravity printing data obtained from parabolic flight tests. Measurements of the Taylor cone both on-ground and in zero-gravity were taken and exploited as a part of the training data. We found that our method obtains good interpolation accuracy (MAPE 3.85%) compared to traditional machine learning methods (MAPE 16.84%) for predicting the printed line width. We concluded that the KRR-HeITL method is well suited for zero-gravity domain shifts of EHD printing parameters. This study paves the way for future predictions of ISM parameters when there are only on-ground experiments or very limited zero-gravity datasets for a given process.

[DOI: 10.1115/1.4066097]

Keywords: inductive transfer learning, domain shift, electrohydrodynamic inkjet printing, in-space manufacturing, additive manufacturing, process engineering, semiconductor manufacturing, sensing, monitoring and diagnostics

1 Introduction

Numerous ongoing research efforts aim to leverage additive manufacturing for in-space applications, with significant contributions from the in-space manufacturing (ISM) efforts led by the National Aeronautics and Space Administration (NASA) [1]. The Additive Manufacturing Facility has been operating aboard the International Space Station (ISS) since 2014. Over 115 tools and components have been created via fused filament fabrication (FFF) of polymers [2,3]. The recent deployment of the first metal 3D printer at the ISS further underscores the commitment to ISM [4]. Before transitioning to in-space operations, all manufacturing processes must undergo validation through zero-gravity experiments, typically conducted via drop towers, parabolic flight campaigns, or sounding rockets. Several additive manufacturing (AM) processes have been validated using these simulated zero-gravity tests including

---

[1] Corresponding author.

Manuscript received April 1, 2024; final manuscript received July 19, 2024; published online September 19, 2024. Assoc. Editor: Ajay P. Malshe.

material extrusion, material jetting, powder bed fusion, direct energy deposition, and vat photopolymerization [5–14]. Conducting on-earth testing of zero-gravity environments is costly and challenging due to the limited testing time. Manned zero-gravity experiments typically last less than 30 s [1], making it difficult to thoroughly explore all operating conditions. There are many emerging AM technologies facing this challenge such as electron beam freeform fabrication [15], FFF [16], and direct-ink write (DIW) [17]. Kauzya et al. [17] studied the structural effects of DIW printing in zero-gravity aboard a parabolic flight and observed differences in structural printing performance. Differences in AM parameters between on-earth and zero-gravity environments present itself as a challenging problem as exploration continues. As emerging additive manufacturing technologies like electrohydrodynamic (EHD) printing gain traction, there is a pressing need to transfer knowledge gained from terrestrial experiments to zero-gravity environments, to accurately predict the printing parameters for in-space operations.

Electrohydrodynamic inkjet printing (EHD printing), an inkjet additive manufacturing technology, is facing this challenge, particularly in in-space environments [18,19]. The first observation of the electrohydrodynamic effect was in the 20th century when Zeleny studied the electrodynamic instability of water droplets under the application of an electric field by using a camera to record images of this phenomenon [20]. Taylor investigated the underlying physics behind this phenomenon and concluded that the process will reach stability when the ink forms a conical shape at the tip of the nozzle, which he coined the "Taylor cone" [21]. The mechanism of EHD printing relies on electrostatic forces to locate and precisely deposit liquid droplets onto the substrate. As an electric field is applied to the nozzle, the electric forces will exceed the surface tension allowing the liquid to form the Taylor cone shape and begin jetting [22]. The formation of the Taylor cone allows the jetted droplets to have a diameter that is much smaller than the nozzle itself. This phenomenon facilitates high-resolution and micro- and nanoscale patterning [23]. EHD printing accommodates a large variety of inks and substrate materials. These materials can be used for biomedical applications like EHD-printed living cells and scaffolds for tissue engineering [23–25]. Conductive inks have been proven effective for EHD-printed micro/nanoscale electronics such as electrodes, nanowires for flexible electronics [26–28], humidity, temperature, and pressure sensors [27–30], transistors, antennas, and light emitting diodes [31–33]. These advantages of excellent compatibility with various inks and substrates while achieving high resolution make EHD printing a promising alternative to traditional electronic manufacturing methods, including lithography, inkjet printing, and screen printing. Additionally, the EHD system is compact, has low energy requirements, and its manufacturing process is straightforward, offering benefits in ease of deployment and maintenance in in-space manufacturing where cargo space and power resources are limited, particularly for frequent and long-duration space missions. Furthermore, EHD printing allows rapid and adaptable prototyping and production of different electronic components while minimizing the material waste. These advantages make EHD printing a promising candidate for in-space manufacturing of electronics. It is important to note that EHD printing is the first thin-film electronic manufacturing method proven printing successfully under zero-gravity conditions.

The precise control of EHD-printed lines is crucial for electronic components, especially considering the high-resolution requirements in space. Achieving stable EHD printing necessitates a meticulous combination of printing parameters. However, accurately modeling the dynamic relationship between these parameters, ink properties, and environmental conditions remains a significant challenge for EHD printing in space. One of the key opportunities is to effectively leverage the knowledge gained from laboratory experiments and apply it to zero-gravity environments. The constraints of zero-gravity testing platforms, characterized by their high costs and short durations, limit the exploration of a comprehensive range of printing parameters. As a result, there is a pressing need for a method to transfer knowledge obtained from laboratory experiments to zero-gravity conditions. Such a method would analyze and expand on the parameters learned under zero-gravity conditions, thereby bolstering confidence in new EHD-printed materials and devices as they transition to in-space experiments.

Machine learning (ML) has played an important role in AM optimization and quality enhancement [34,35]. Its algorithms can perform both explanatory and predictive tasks allowing it to capture the complex relationships between the printing parameters (features) and the final output (target). ML has been used to model design parameters, operating parameters, material characteristics, as well as other environmental conditions on AM methods. Several studies used machine learning algorithms to predict the droplet diameter and ejection frequency of the EHD printing system [36,37]. ML can also be used alongside machine vision to facilitate defect mitigation and in situ control of AM. Machine vision for characterization and in situ control has been implemented in many AM technologies, such as FFF [38,39], direct-ink write [40], and inkjet printing [41]. Machine vision has also been used in various studies and simulations of EHD printing as well [42]. Taylor cone measurements via machine vision have assisted with the characterization and quality of EHD printing [41–43]. Substrate imaging has been used to implement in situ jet-speed monitoring of EHD spraying and EHD-printed droplets [37,42]. Lies et al. used machine vision to detect and measure EHD filament printing [44]. ML alongside machine vision allowed the classification of the jetting status of EHD Taylor cones [45,46].

ML and machine vision offer promising ways to optimize the printing process on the ground. However, another technology is still needed to leverage this knowledge to zero-gravity conditions. One method for combining knowledge across domains is transfer learning (TL). TL is an extension of ML where ML is traditionally performed within the data's domain using the same features and targets, whereas TL's algorithms are trained on one dataset, and that knowledge is leveraged to make predictions on a related task [47]. Instead of starting the learning process from scratch, the learned model is transferred and fine-tuned so that it can be applied to a dataset where the amount of labeled data is scarce or expensive to obtain. It aims to improve the learning performance and reduce the computational time by training less labeled data as well [48]. As seen in Fig. 1, the type of transfer learning method to employ depends heavily on the characteristics of the used data. TL problem settings are categorized according to Pan and Yang [49] as inductive, transductive, and unsupervised. Generally speaking, inductive settings indicate when labeled data is available on the target domain. Transductive settings refer to when labeled data is only available on the domain. Lastly, unsupervised TL refers to when labeled data is unavailable in both source and target domains. Methods can further be categorized as heterogeneous or homogeneous, which refers to whether the features between sources or between sources and targets are the same. This labeling notation can also be used to classify whether the data sources and target are from the same or different domains. After data characterization, a decision is made about what information to transfer between data domains. These methods can be classified as instance-based transfer, feature-representation transfer, parameter transfer, and relational-knowledge transfer. Simply speaking, instance-based transfer uses reweighting of the source data to determine which observations contribute positively to the target domain. Parameter transfer assumes the sources and target share the same or similar distribution of model hyperparameters, so that the parameters themselves can be shared between datasets. Relational-knowledge transfer is the sharing of logical rules or relationships between the source and target domains. Finally, in feature-representation transfer, the intent is to learn a feature representation so that knowledge can be encoded to the target domain. It can be further categorized as symmetric and asymmetric. Asymmetric methods adjust the source features to align with the target features, while symmetric methods aim to identify a shared latent feature space and subsequently transform both the source and target features into a

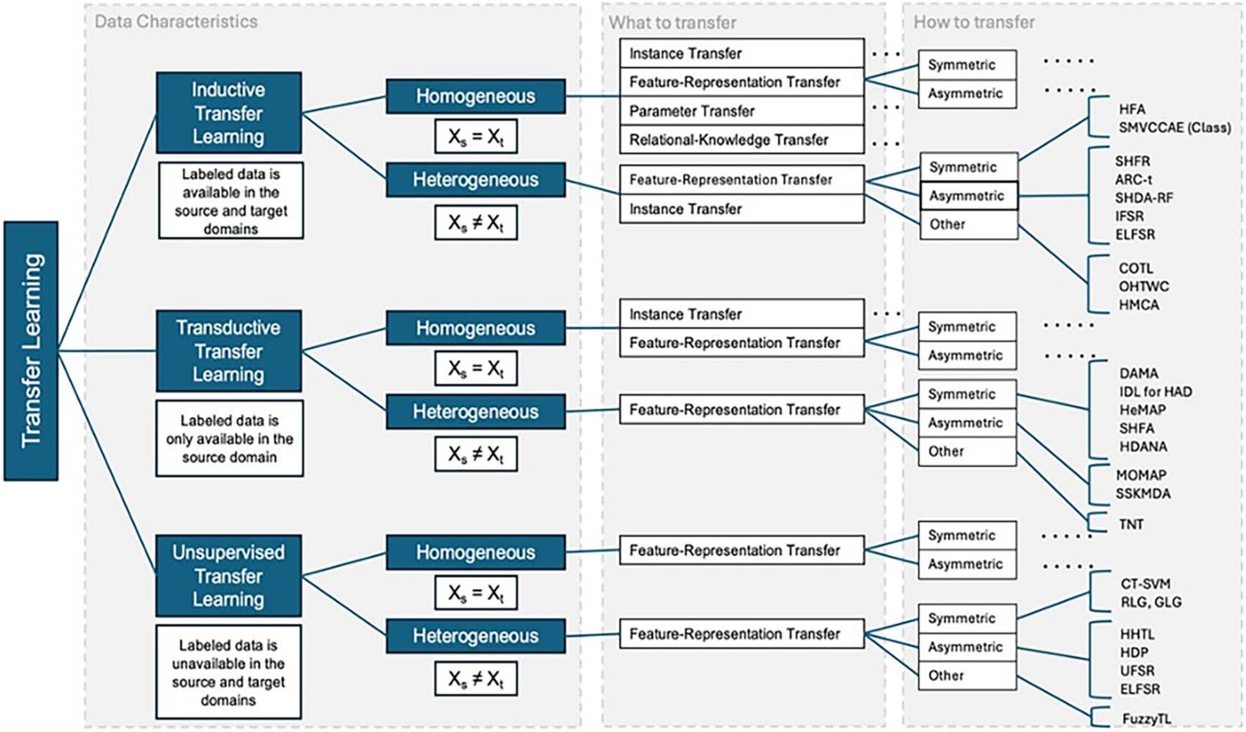

Fig. 1 The categorization of transfer learning methods

unified feature representation [48,50]. Transfer learning has some notable applications including object detection in machine vision, aero engine fault diagnosis, autonomous driving, and healthcare applications such as medical image analysis and disease prediction [47–49,51,52]. Transfer learning has also been extensively studied within the additive manufacturing field where various printing parameters have been transferred across AM methods, materials, and equipment [53–55].

Transfer learning holds immense potential in the context of space exploration, particularly given the limitations of current zero-gravity testing platforms, which are both costly and short in duration. Despite its evident value, the effectiveness of transferring knowledge between terrestrial and in-space environments has been inadequately studied. While Waisberg et al. [56] highlight the potential of transfer learning in space medicine, focusing on the scarcity of astronaut medical data, Ogundipe and Ellery [57] delve into its application in mitigating differences between earth-based and space-based dynamics of robotic manipulators used for capturing space debris. Surprisingly, these are among the few publications addressing knowledge transfer from terrestrial to zero-gravity environments.

In summary, the rapidly developing field of in-space manufacturing presents increasing requirements for effective production methods. As one of the emerging additive manufacturing technologies, EHD printing has proven to be effective for printing without gravity and shows promise for electronics printing in space. However, various limitations hinder optimization based solely on zero-gravity experiments. Therefore, it is urgent and necessary to find a method that can leverage the knowledge gained from ground-based research to apply to in-space conditions. Thus, we proposes a heterogeneous transfer learning method tailored for AM physics-based parameters, aiming to predict printing outcomes in zero-gravity environments. The organization of this paper is as follows: Sec. 2 delves into the fundamentals of the EHD printing process and introduces the data collected from both on-ground and zero-gravity experiments. Section 3 highlights the incorporation of machine vision as a feature in EHD printing data analysis. In Sec. 4, traditional machine learning approaches are explored, followed by an explanation of the proposed transfer learning method in Sec. 5. Finally, Sec. 6 presents the prediction results obtained through the proposed methodology.

2 Electrohydrodynamic Printing and Validation Experiments for In-Space Manufacturing

EHD is an inkjet additive manufacturing method in which electrical force drives the liquid flow. The complex physics behind the EHD printing process is dictated by the relationship of a large number of parameters. The quantity of these parameters and their interactions with each other make EHD printing a challenging process to control. Furthermore, under zero-gravity conditions, most of the operating conditions experience a domain shift to achieve stable jetting. EHD printing has also been the topic of zero-gravity-related research [18], so there is sufficient data available for transfer learning on this topic. Therefore, EHD printing is the selected candidate for this work. The voltage of the applied electric field to the nozzle is one of the parameters that control the stability of the printing. As the voltage increases, the ink is drawn downward into the cone shape and begins jetting. To achieve the desirable cone-jet stage, a precise selection of printing parameters and ink properties is crucial. EHD printing parameters include applied voltage, duty ratio, frequency, standoff distance, nozzle diameter, and pressure. Ink characteristics such as density, viscosity, surface tension, and conductivity also play a major role. Finally, environmental conditions, such as humidity and temperature, play a role in the physics of EHD printing. The process parameters include the applied voltage V, the standoff distance between the tip of the nozzle and the substrate h, the nozzle diameter d, and the speed of printing s. Ink properties determine how these printing parameters interact with each other, and they include the printed line pattern width W. A detailed report on the physics of EHD printing can be found in our previous publication [36].

Three EHD printing experiments were completed, two of which were completed on-ground in the lab, and the third was completed on a parabolic flight. The EHD printer hardware consists of the

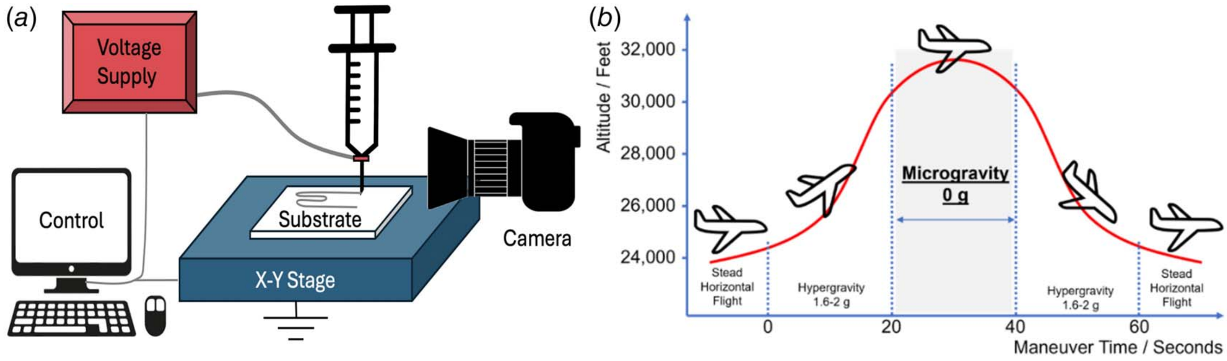

Fig. 2 Schematic drawing of the (*a*) EHD printing setup and (*b*) depiction of the parabolic flight maneuver

following elements depicted in Fig. 2(*a*): the printhead, power supply, *x*–*y*–*z* stages, ink supply, nozzle, and control software. A syringe is used to house the ink supply and is connected to a metal ink reservoir, which is connected to a conducting electrode, encased by a glass nozzle. The power supply generates a high-voltage electric field to the electrode on the nozzle. To mitigate printing vibrations during flight, the nozzle is fixed on the *X*–*Y* plane, and two microstages enable a maximum plotting speed of 20 mm/s within a 100 mm by 100 mm travel range. A high-speed camera allows the viewing and recording of the nozzle tip and Taylor cone at 20,000 frames per second (fps).

The first experiment varied the following parameters: the printing speed, standoff distance, and applied voltage. Printing was performed using a fixed nozzle diameter of 50 μm. The goal was to investigate these parameters' effect on the resulting line width, which is the target of this study. Commercial silver Novacentrix water-based nanoparticle 40 wt% ink was used in this experiment. DC pulse was the type of voltage applied. High-speed videos also captured the Taylor cone formation and jetting, and its height and angle were measured (details in the next section). Table 1 summarizes all experiment features and ranges. The second experiment expands this dataset while printing via AC voltage, thus parameters of duty ratio, frequency, and applied voltage were varied. The nozzle diameter, standoff distance, and printing speed were kept constant. A 35 wt% Ag nanoparticle ink was used. The goal is to transfer knowledge that is learned from these on-ground experiments to interpolate data obtained in zero gravity. The final experiment was conducted on parabolic flight campaigns in December 2020. A parabolic flight test, also known as a parabolic flight campaign or parabolic flight maneuver, is a method used to simulate microgravity or zero-gravity conditions for short durations on earth. This technique involves flying an aircraft along a parabolic trajectory, during which the aircraft ascends steeply, levels off, and then descends steeply, as shown in Fig. 2(*b*). During the ascent phase, the aircraft generates a pull-up force that can briefly counteract the effects of gravity, resulting in a period of weightlessness or reduced gravity within the cabin. This state is "zero-g" and typically lasts for about 20 s per parabola. We assume this simulates the full effect of zero gravity in an actual in-space manufacturing environment. The EHD printing parameters in zero-gravity are also summarized in Table 1. A 100-μm nozzle was used with AC voltage, while voltage and frequency were varied. Due to the short periods of zero gravity, a small number of successful parameter combinations were tested.

3 Data Processing: Machine Vision

In EHD printing, it has been observed that notable differences can be seen on the Taylor cone from changes in voltage, frequency, duty ratio, standoff distance, and the material being printed [21]. Furthermore, we have observed that the Taylor cone height and angle are smaller in zero gravity while printing using the same parameters. These physical differences can provide clues about the volume of material ejected and therefore the resulting line width [58]. To exploit these differences, we developed a machine vision system to measure the Taylor cone profile during printing. Because of the differences in lighting while printing, the method is adaptable so that it extracts the highest resolution of Taylor cone jetting possible. Various techniques using the *OpenCV* library in PYTHON have been implemented and are highlighted in the next sections.

3.1 Region of Interest Identification. The region of interest (ROI) contains the Taylor cone and must be identified in an accurate and consistent way. Before applying the voltage, an image of the

Table 1 Range of EHD printing parameters for on-ground experiments and parabolic flight experiments

Parameter	Ground experiment 1	Ground experiment 2	Parabolic flight experiment	Function in model
Voltage (V)	600, 700, 800, 900, 1000, 1100, 1200	700, 750, 800, 850, 900, 950, 1000	2100, 2150, 2200, 2550, 2850	Input
Duty ratio (%)	NA	5, 10, 15, 20, 25, 30	60	Input
Frequency (Hz)	NA	1, 5, 10, 70, 80, 90, 100, 150, 200, 250, 300	50, 100	Input
Nozzle diameter (μm)	50	75	100	Input
Plotting speed (mm/s)	5, 10, 15	10	2.5	Input
Standoff distance (μm)	75, 100, 125	187.5	18.12–111.74	Input
Ag ink loading (wt%)	40	35	35	Input
Taylor cone height (μm)	15.05–45.30	NA	20.39–50.66	Input
Taylor cone angle (deg)	45.19–57.74	NA	24.64–45.35	Input
Line width (μm)	14.48–149.53	30.86–60.48	41.48–120.08	Output

nozzle without the Taylor cone is taken. The images without jetting serve as a reference for cropping the ROI, which will only contain the Taylor cone. We use an adaptive threshold to handle variations of lighting and contrast to return a binary image and mitigate the effect of noise. We then identify the nozzle tip to serve as the top reference points to the ROI. The ROI is then identified as seen in Fig. 3.

3.2 Measurement of Taylor Cone Height and Angle. The feature of "drop-on-demand" in EHD indicates that the Taylor cone will pulse over time as droplets are released. The frequency of droplets can be upwards of hundreds/second, which usually requires the use of a high-speed camera to effectively capture a "jet." The Taylor cone contour was located and its vertexes were used to measure the Taylor cone height of each frame. The largest height was then recorded for each period as the height of that jet as depicted in Fig. 4. The height of the Taylor cone jets was averaged over each set of parameters. The angle was also measured between the left-most point and the jet of the Taylor cone. This angle is symmetric, so only one side is measured, and again averaged over each set of parameters.

4 Traditional Machine Learning Approaches

In traditional machine learning methods, a dataset consists of data points $X \subset \mathbb{R}^{N \times D}$ and their corresponding labels $Y \subset \mathbb{R}^{N}$. It is assumed that these data points follow a distribution $p(x, y)$ that stays constant over time, even for new data. According to this assumption, a model trained on X and Y should perform well on new data as well. However, this assumption may not always hold true. For example, a model trained to predict rainfall based on environmental conditions in Northern California will likely not be able to make accurate predictions for Southeast Asia even if the features are the same. In our case, a machine learning model that is trained on data obtained from ground experiments, will likely not perform well on zero-gravity parabolic data because we suspect the underlying distribution and range of physics-based parameters are different. Nonetheless, as one of the pioneering works in the field of zero-gravity transfer learning, we tested traditional machine learning methods to prove their inadequacy for this problem. All data processing, modeling, and analysis were performed using PYTHON.

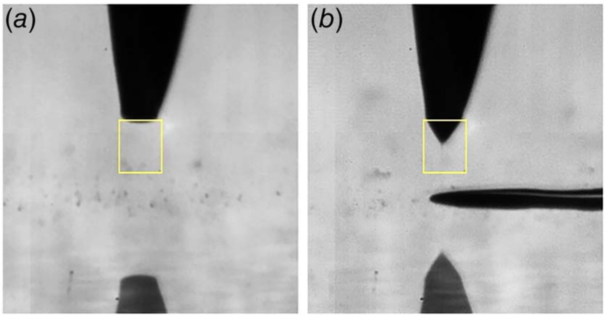

Fig. 3 (*a*) ROI identification during no jetting phase and (*b*) Taylor cone and jetting captured. Reflective nozzle images were in the view because the printing was on glass substrates.

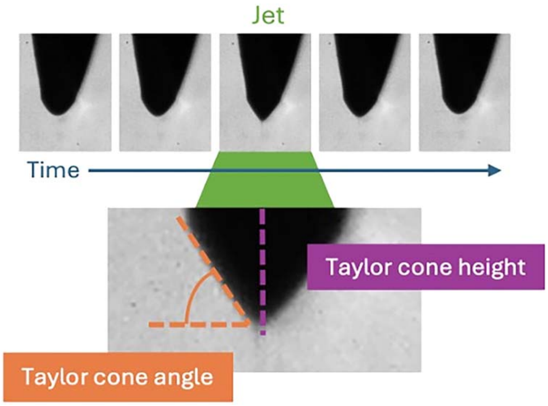

Fig. 4 Measurements of the height and angle of the Taylor cone

4.1 Training Data for Traditional Machine Learning. The ground and parabolic flight printing parameters and Taylor cone measurements in Table 1 were used as features to predict the target, printed line width. The set of input features of the baseline and transfer learning models contain the operational printing parameters including the applied voltage, duty ratio, frequency, nozzle diameter, plotting speed, standoff distance, and Ag ink loading. Additionally, it contains Taylor cone measurements observed during the printing process obtained via machine vision consisting of Taylor cone height and Taylor cone angle. These inputs are used to predict the target feature, which is the printed line width (see Table 1). The two on-ground experiments were used as training data and contain 254 data points. The parabolic flight experiment contained nine data points, three of which were used for training and the remaining 6 were used for testing. To help compensate for the suspected domain shift between on-earth and zero-gravity printing parameters, we added the minimum, median, and maximum line width points of the parabolic flight data to the training data to assist the model in making predictions about the new ranges of the printing parameters in zero gravity. The remaining 6 points were used for testing. A schematic representation of the data sources, features, and transfer learning mechanism can be seen in Fig. 5. Prior to training, standardization was performed using the MinMax scaler. A visualization of the locality and spread can be seen in Fig. 6. We observed that slightly different parameters were required to print the same range of line widths in zero gravity.

4.2 Evaluation Metrics. To evaluate the performance of each model we will compute the root mean squared error (RMSE), coefficient of determination (R^2), mean squared error (MSE), and mean absolute percentage error (MAPE) between the actual and predicted line widths of the training and testing data:

$$\mathrm{RMSE} = \sqrt{\frac{\sum_{i=1}^{n} (y_i - \widehat{y_i})^2}{n}} \tag{1}$$

$$R^2 = \left(\frac{\sum_{i=1}^{n} (y_i - \bar{y}_i)(\widehat{y_i} - \bar{\widehat{y}}_i)}{\sqrt{\sum_{i=1}^{n} (y_i - \bar{y}_i)^2} \sqrt{\sum_{i=1}^{n} (\widehat{y_i} - \bar{\widehat{y}}_i)^2}} \right)^2 \tag{2}$$

$$\mathrm{MSE} = \frac{1}{n} \sum_{i=1}^{n} (y_i - \widehat{y_i})^2 \tag{3}$$

$$\mathrm{MAPE} = \frac{1}{n} \sum_{i=1}^{n} \left| \frac{y_i - \widehat{y_i}}{y_i} \right| \times 100\% \tag{4}$$

Note that the subscripts are all "i" in Eqs. (1)–(4), though some looked like "l."

Here, n represents the number of samples, y_i and $\widehat{y_i}$ are the target and model outputs, $\bar{y}_i$ is the mean of the target line widths, and $\bar{\widehat{y}}_l$ is the mean of the predicted line widths. RMSE is measured in μm as the EHD-printed lines are in the microscale.

4.3 Baseline Machine Learning Models. In this study, three artificial neural network (ANN) models using 3, 5, and 10 layers

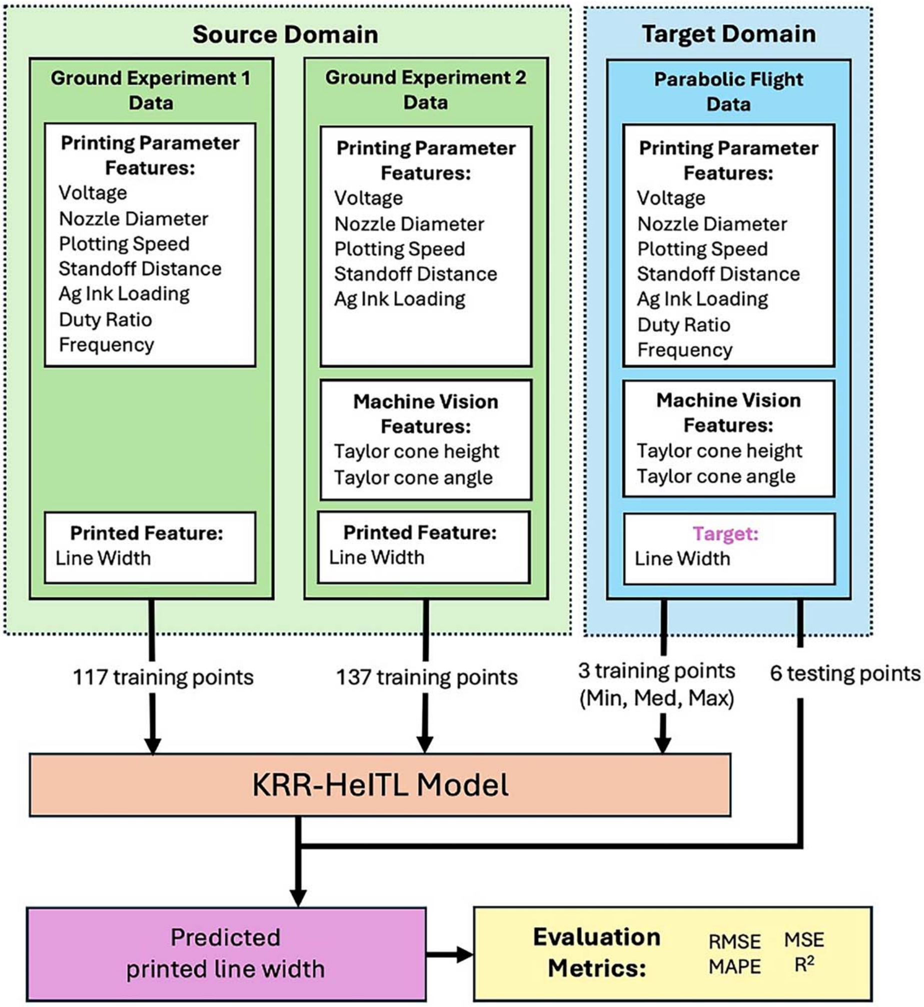

Fig. 5 A schematic of the data sources, features, and transfer learning mechanism

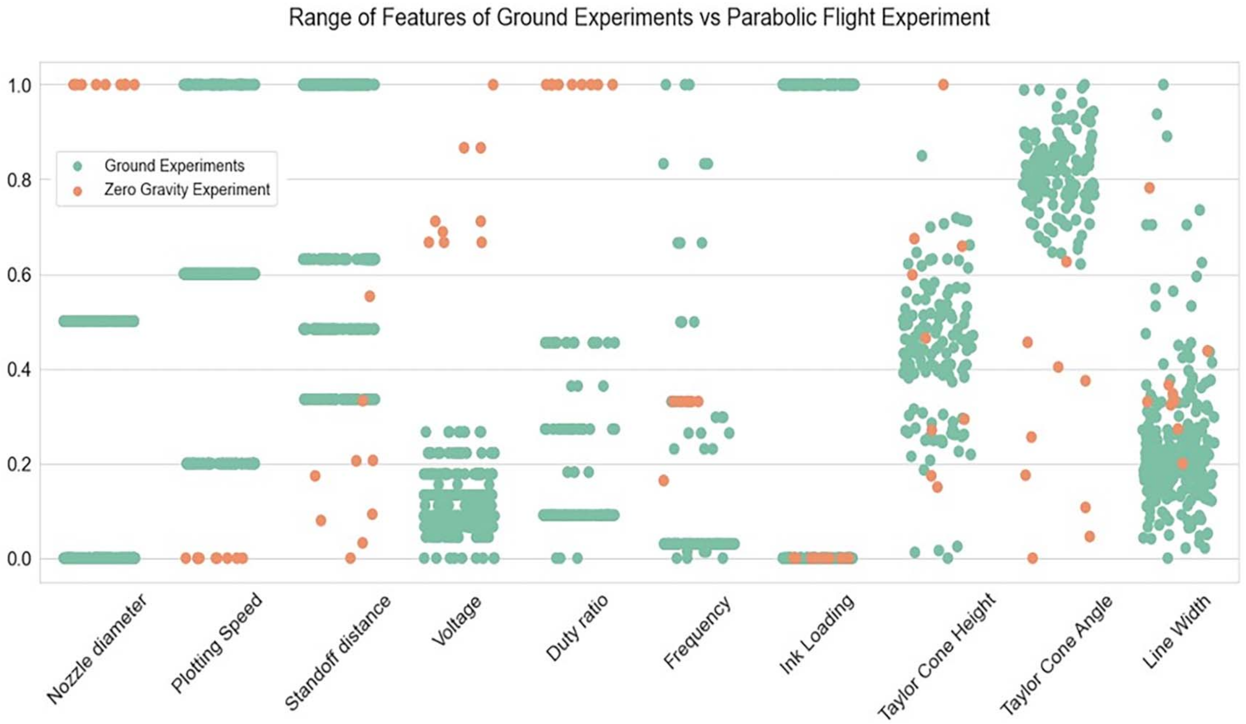

Fig. 6 Boxplot of scaled features of the ground experiments (green) and the parabolic flight experiment (orange)

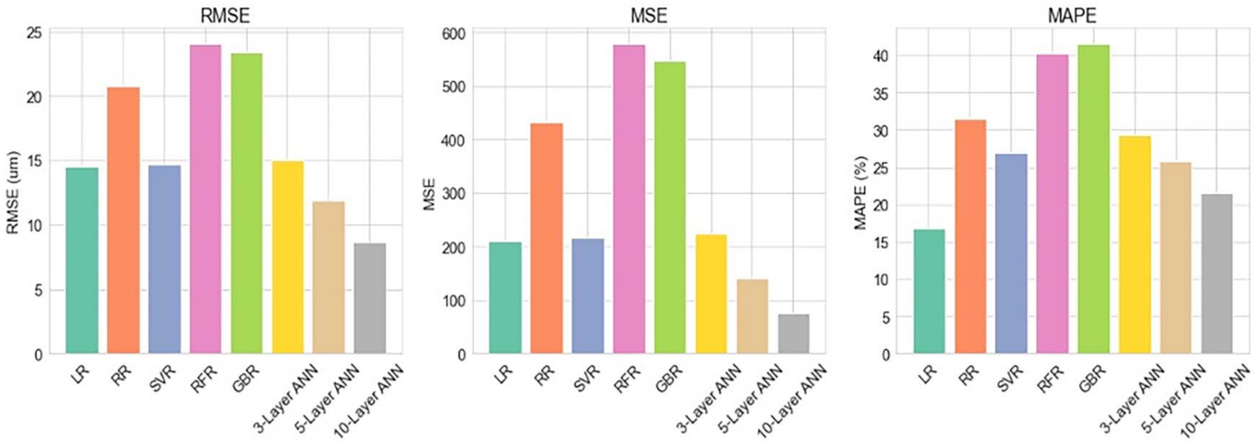

Fig. 7 Results of traditional (baseline) machine learning models

were tested. We used the Hyperopt package to optimize the hyperparameters of each individual model by minimizing the RMSE. All machine learning was performed using scikit-learn v1.3.1. The following methods were employed: linear regression (LR), ridge regression (RR), support vector regression (SVR), random forest regression (RFR), gradient boosting regression (GBR), and ANN. Each method is briefly described: (1) LR is a simple statistical model used to predict a continuous target variable by fitting a linear relationship between the input features and the target. (2) RR is a linear regression technique that adds a penalty term to the ordinary least squares method, helping to mitigate multicollinearity and overfitting by shrinking the coefficients toward zero. (3) SVR is a supervised learning algorithm used for regression tasks that aims to find the optimal hyperplane in a high-dimensional space to minimize the error between the predicted and actual values. (4) RFR is an ensemble learning method that builds multiple decision trees during training and outputs the average prediction of the individual trees, providing robustness against overfitting with high prediction accuracy. (5) GBR is an ensemble learning technique that builds a series of weak learners (here we use decision trees) sequentially, with each tree trained to correct the errors of its predecessor, resulting in high predictive accuracy. (6) ANN is a computational model consisting of interconnected nodes (neurons) organized in layers, used to learn complex patterns and relationships in data for regression tasks.

4.4 Results of Baseline Machine Learning Models. The results of the baseline models could be seen in Fig. 7. It can be observed that the models did not perform well on the zero-gravity data. The best models were LR and the 10-layer ANN which had RMSE and MAPE values of 14.52% and 16.84% and 8.66% and 21.57%, respectively. In the context of our problem, we targeted a MAPE below 10% based on other reported research on transfer learning in the AM domain [53,54]. Furthermore, the R^2 values for all models were negative indicating that the models are poorly fit and fail to explain the variance within the data. This can be attributed to the dataset shift of the physics-based features that are not being adequately treated within the traditional machine learning models. Thus, transfer learning was utilized to address this problem.

5 Transfer Learning Approach

As mentioned above, we observed a dataset shift in feature spaces from on-earth to zero-gravity data. Mathematically speaking, the distribution of the on-earth (or E) data was different from the distribution of the zero-gravity, "in-space" (or S) data in the covariate x and dependent variable y: $p^E(x, y) \neq p^S(x, y)$. We assumed that the distributions of the E data and the S data are similar to a certain extent; however, compensating for this difference with a small number of S data points was challenging. In other words, the challenge faced by all ISM processes is how we could leverage a large amount of on-earth data from a certain domain with a small amount of in-space data from a different domain to make predictions. Our data contained labels in the source and target domains; however, the domains themselves were different; this was defined as a *heterogeneous, inductive transfer learning (HeITL)* problem [59]. Several models could be selected to address this problem. The Supervised Heterogeneous Transfer Learning model by Sukhija and Krishnan [60] could be a candidate; however, we did not wish to apply labels to our data, since our testing data is so scarce. For the same reason, we did not wish to unify different feature spaces like Shi et al. [61] did in the Heterogeneous Spectral Mapping transfer learning model. Finally, the dimensionality of our data did not call for a deep learning model nor one specialized for high-dimensional data such as image classification or the Oracle Trans-Lasso model by Li et al. [62]. The model we employed was weighted kernel ridge regression (KRR) for HeITL and a full derivation could be found by Garcke and Vanck [59]. An instance-based transfer approach was selected because it is adaptable to multisource training data that contains different features among them. Typical regression models do not allow the sharing of different feature spaces. Thus, we employed importance-based weights to allow the transfer of information between multiple different data sources that contain different features. Each instance of the E data was assigned a weight based on its perceived value in predicting the S target. The optimized weights were then used in a ridge regression model, which used the E data and some of the S data to interpolate the remaining S targets. This model was selected because of its three characteristics: it can utilize datasets that contain different features, it can compensate for the domain shifts among those features, and data from future experiments can be added sequentially to support training the model.

5.1 Weighted Kernel Ridge Regression for HeITL. We introduce the two datasets (X^E, Y^E), the E data collected on-earth, and (X^S, Y^S), the S data collected in zero-gravity "space." These are given by

$$(X^E, Y^E) \sim p^E(x, y) \quad \text{and} \quad (X^S, Y^S) \sim p^S(x, y) \tag{5}$$

where $|X^S| < < |X^E|$, i.e., $M << N$, and M represents a small subset of S data that will be used in training denoted by S_r . The remaining subset will be used for testing, denoted by S_t . The distributions of both sets of data were assumed to be related but not equal, i.e., $p^E(x, y) \neq p^S(x, y)$.

First, only using the E data, we learned the model coefficients a_E for normal kernel ridge regression by minimizing the regularized squared loss function:

$$\min_{f \in H} \frac{1}{N} \sum_{j=1}^{N} (y_j - f(x_j))^2 + \lambda ||f||_H^2 \tag{6}$$

by using the kernel trick and taking the dual:

$$\min_{a_E} \frac{1}{N} (a_E^T K a - 2a_E^T y + y^T y) + \lambda a_E^T K a \tag{7}$$

where λ represents the regularization parameter, and the kernel used is the Gaussian radial basis function (RBF), i.e., $k(x, y) = \exp(-(||x - y||^2 / 2\sigma^2))$, where σ denotes the bandwidth hyperparameter. Using the estimated model coefficients a_E obtained only using the E data, we estimated the weights $\hat{w}$ of each point j in N via a linear combination of Gaussian kernels:

$$\hat{w}_j^{a_E}(x_j^E, y_j^E) = a_{Ej} \exp\left(-\frac{||(x^{S_r}, y^{S_r}) - (x_j^E, y_j^E)||^2}{2\eta^2}\right) \tag{8}$$

where η is the kernel width parameter and (x^{S_r}, y^{S_r}) is a data point from the training set S_r. The weights form the diagonal matrix $\widehat{W} \in \mathbb{R}^{(N+M)\times(N+M)}$:

$$\hat{W} := \begin{bmatrix} I_{N+M} & 0 \\ 0 & \operatorname{diag}\left(\hat{w}(x_1^E, y_1^E), \ldots, \hat{w}(x_N^E, y_N^E), \widehat{w}(x_1^{S_r}, y_1^{S_r}), \ldots, \hat{w}(x_M^{S_r}, y_M^{S_r})\right) \end{bmatrix} \tag{9}$$

for each training point i in S_r. The prediction function could now be derived using the discriminative case of a standard machine learning model:

$$\hat{y}^\star = \operatorname{argmax}_y p(y|x^\star) \tag{10}$$

where $x^\star$ represents a new data point we want to predict, in our case from a testing set S_t, and $\hat{y}^\star$ is the prediction. To estimate $\hat{y}^\star$, we use Gaussian kernel ridge regression:

$$\operatorname{argmax}_y p(y|x^\star) \approx f(x^\star) = a^t k(x^\star) \tag{11}$$

where $k(x^\star) := (k(x_1, x^\star), \ldots, k(x_{N+M}, x^\star))^t$ is the kernel map of $x^\star$ on the training data E and S_r, and a is a vector of coefficients. The approximation could now be taken as a function of the weights:

$$\operatorname{argmax}_y (\hat{w}(x^\star, y) p(y|x^\star)) \approx f_{\hat{w}(x^\star, y)}(x^\star) = a^t \hat{W}(x^\star, y) k(x^\star) \tag{12}$$

plugging this into the regularized squared loss function, and replacing $(x^\star, y)$ with a point from the features space we want to predict S_r we obtain the following convex optimization problem:

$$\min_{\alpha \geq 0} \sum_{i=1}^{M} (y_i^{S_r} - a^t \hat{W}^\alpha(x_i^{S_r}, y_i^{S_r}) k(x_i^{S_r}))^2 + \gamma ||\alpha||^2 \tag{13}$$

λ again represents the regularization parameter. The λ values represent regularization parameters, and they are optimized relative to each equation (e.g., λ values in Eqs. (7) and (13) are optimized separately). The optimized coefficient vector α defines the weights $\hat{w}$, which will be used in the final modified ridge regression model:

$$J(\theta) = \frac{1}{2}\left(\sum_{i=1}^{M} (\theta^t \phi(x_i^{S_r}) - y_i^{S_r}\right)^2 + \sum_{j=1}^{N} \widehat{w}_j(\theta^t \phi(x_j^E) - y_j^E)^2) + \frac{\lambda}{2} \sum_{d=1}^{D} \theta_d^2 \tag{14}$$

where θ denotes the model parameters, ϕ is the feature map, λ is the regularization parameter, and D is the number of features. As already implied, the E and S_r datasets are vertically concatenated as well as the Gaussian kernel matrix, K:

$$X^{ES_r} = (X^E | X^{S_r}) \quad \text{and} \quad Y^{ES_r} = (Y^E | Y^{S_r}) \tag{15}$$

$$K = \phi(X^{ES_r})^t \phi(X^{ES_r}) \tag{16}$$

where $X^E \in \mathbb{R}^{N\times D}, X^{S_r} \in \mathbb{R}^{M\times D}$ and labels $Y^E \in \mathbb{R}^N, Y^{S_r} \in \mathbb{R}^M$. Taking the dual we obtain

$$\frac{1}{2} a^t K W K a - a^t K \hat{W} Y^{ES_r} + \frac{1}{2} Y^{ES_r} + \frac{\lambda}{2} a^t K a \tag{17}$$

The Gaussian RBF is used here; the bandwidth hyperparameter is denoted by σ. Once the optimal model parameters a have been found, a new prediction on the test set $\hat{y}^{S_t}$ can be found using

$$\hat{y}^{S_t} = \sum_{l=1}^{N+M} a_l y_l k(x_l^{ES_r}, x^{S_t}) \tag{18}$$

The supervised KRR-HeITL approach required the estimation of bandwidth parameters η and σ and regularization parameters λ and γ. The additional regularization term allows higher control of the optimization across combined datasets. Additionally, KRR-HeTL heavily leverages S_r labels to compensate for the dataset shift resulting in robust predictions of S_t.

5.2 Data for KRR-HeITL.

To test the effectiveness of the transfer learning model on the zero-gravity data, we considered 4 different sets of training data. All included the on-ground experiment data, but the number of zero-gravity data points differed. The first was the same as the baselines in Sec. 4.1: we included the minimum, median, and maximum points of the zero-gravity data in our training set [Min, Max, Med]. We tested only including the minimum and maximum points [Min, Max], only including median [Med], and using the tertiles [Tert]. The Med and Tert models were used to test how our model performs on extrapolating the data, while the others were tested on interpolation. By giving the model a range of which parameters are shifted and by how much, the model can better interpolate the remaining points.

Naturally, there is a large imbalance in the number of points in training and testing sets since we are testing the model on data collected during parabolic flight tests (254 points to train and only 9 points to test). A commonly used method to deal with data imbalance is to oversample our noncomplete dataset to rebalance it [63]. However, such oversampling usually requires a thorough understanding of the correlation, uncertainty, and the structure of the dataset [64]. Otherwise, the rebalancing performance will be impaired. Unfortunately, the transfer learning between on-ground and in-space EHD printing is an emerging research topic, and the required understanding is not satisfied. This explains why we directly deal with the imbalanced dataset to test the KRR-HeITL model. Nevertheless, in the future, this model may be used to interpolate more points than the quantity obtained via parabolic flight tests. To broaden our results to larger amounts of testing data and address this imbalance, some commonly used data augmentation methods were tested as benchmarks. Three data simulation techniques were tested: the Generative Adversarial Network (GAN), Wasserstein GAN (WGAN), and Variational Autoencoder (VAE). Each was used to simulate 100 new data points for testing. These new data imitate a nearly 70% and 30% training testing split. The GAN is a common and effective way of generating new data by using competing neural networks to create realistic simulated data from small training sets. The VAE can learn the distribution of the data and generate new points based on sampling from the learned latent space. In this case, the parabolic flight data are input, and the simulators are used to produce 100 new data points from the zero-gravity distribution for use as the simulated test set. Ten sets of simulated data are generated and the average MAPE, MSE, RMSE, and R^2 values of the KRR-HeITL model are reported in Table 2.

5.3 KRR-HeITL Results and Discussion.

This section presents the results of the transfer learning model, KRR-HeITL, and compares it to the baseline machine learning models presented above on the original, unmodified parabolic flight test data. The

Table 2 RMSE, R^2, MAPE, and MSE of the model tested on the original parabolic flight data ([Min, Med, Max], [Min, Max], [Med], and [Tert]) and of the model tested on simulated data using GAN, WGAN, and VAE

Training data	Model	RMSE	R^2	MAPE	MSE
Original parabolic flight data	[Min, Med, Max]	2.88	0.82	8.27	3.85
	[Min, Max]	2.92	0.78	8.53	4.05
	[Med]	44.75	−3.07	2002.9	53.00
	[Tert]	45.24	−2.86	2016.8	51.16
Simulated data	GAN + [Min, Med, Max]	11.60	0.54	12.71	134.64
	WGAN + [Min, Med, Max]	10.41	0.59	8.82	108.42
	VAE + [Min, Med, Max]	25.00	−0.75	27.72	625.09

results of the KRR-HeITL model on the four different training datasets can be found in Fig. 8. Directly comparing the results of training on the [Min, Max, Med] dataset, the best MAPE was 16.84% using the baseline LR model, while the KRR-HeITL model obtained 3.85%. The smallest RMSE of the baseline models was 8.66 μm by the 10-layer ANN, while KRR-HeITL obtained 2.88 μm. However, when comparing these results, it is important to note that the baseline models all had negative R^2 values indicating they did not explain the variability exhibited by the zero-gravity data. The KRR-HeITL model obtained an R^2 value of 0.82, meaning 82% of the variability in the zero-gravity data was explainable by the model. This marked a significant improvement over the baseline machine learning models, which did a poor job of explaining the shift in the feature domains.

Next, we compared the performance of the KRR-HeITL model across different sets of training data to understand its limitations. The [Min, Max] training set obtained comparable results to the [Min, Max, Med] training set, with an RMSE of 2.92 μm and a MAPE of 4.05%. The R^2 was slightly lower at 0.78. Both [Min, Max, Med] and [Min, Max] training sets achieved a MAPE of less than 5%, and we consider this to be acceptable for use in practice. As mentioned above, the EHD printing process depended on environmental factors as well, such as temperature and humidity, so even while using the same ink and printing parameters, the printed line widths may be slightly different. Based on our experiments, we found that the variability between day-to-day printed line widths was around 5%, thus validating the success of the KRR-HeITL model for interpolating on-ground knowledge to zero gravity for EHD physics-based parameters. The Med and Tert training sets test the model's ability to extrapolate EHD-printed line widths beyond what the model was trained on. The Med and Tert models obtained a MAPE of 53% and 51%, respectively, showing that they cannot adequately predict line widths beyond the range of zero-gravity data they are trained on. In this study, we concluded the KRR-HeITL model performs well for interpolation of zero-gravity line width data, but it cannot extrapolate its predictions accurately.

Next, we simulate more testing data for the [Min, Med, Max] method using the GAN, WGAN, and VAE since the quantity of our zero-gravity data is limited. The results can be found in Table 2. Using 100 simulated test points across 10 folds, the KRR-HeITL model achieved the best average MAPE of 8.82%, an MSE of 108.42 μm^2, an RMSE of 10.41 μm, and an R^2 of 0.59 using WGAN simulated data. This performance is worse using simulated data than using the real zero-gravity data. We suspect this could be due to several factors. First, the data simulators may produce data that lacks the finer details, complexities, and patterns that may be difficult to replicate. Furthermore, GANs have been reported to introduce bias in small training samples [65]. The model also may contribute noise that does not exist in the real data, specifically in instances where some features are marginally or jointly distributed, such has been reported in other physics-motivated processes [66]. Although the model does not perform as well on GAN-simulated data, to draw a proper conclusion, we

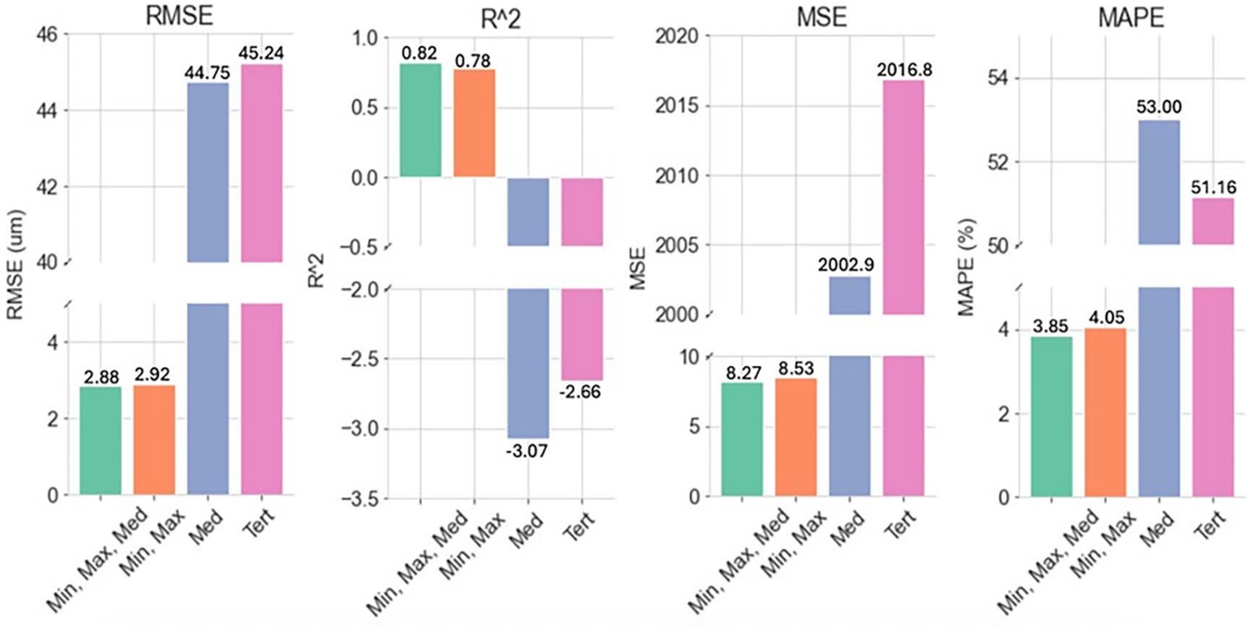

Fig. 8 Results of the transfer learning model on training groups (Min, Max, Med), (Min, Max), Med, and Tert

recommend the following research topics as future works: a thorough study of the correlation, uncertainty, and distribution of the data so that an oversampling technique can be properly applied, and the use of a simulation specifically designed for EHD physics to fabricate more samples.

To improve the accuracy and R^2 of our model, we plan to add new on-ground data to the training set as more data from experiments is collected. A strength of our instance-based model was that data can be added iteratively and reweighted according to its relevance to the zero-gravity data. In the future, we would like to gather EHD printing data from existing publications to further expand the training data. As more parabolic and in-space data become available, we will perform further testing on this model to verify its accuracy. Of all the transfer learning strategies that have been published, we selected one and demonstrated its effectiveness on the ground-to-space transfer. However, many other models may be acceptable and would likely out-perform KRR-HeITL. KRR-HeITL is an instance-based transfer of data, but the domain shifts of the features also suggest a feature-based approach may perform well too. There is also great potential for transfer learning models that are developed with the sole purpose of ground-to-space transfer of physics knowledge. To our knowledge, this study is one of the first steps in realizing transfer learning for the transfer of terrestrial data to "in-space" applications. We gladly invite more research on this topic as we see the growing commercialization of space.

6 Conclusion

This research explores the potential of transfer learning to be used for predicting EHD-printed line widths under zero-gravity conditions. The EHD printing process is dominated by physics, so its printing parameters experience a domain shift under zero-gravity conditions. We demonstrate that traditional machine learning methods cannot compensate for this domain shift, so we test a transfer learning method, KRR-HeITL, built for handling heterogeneous data. Using two EHD printing datasets collected from on-ground experiments, and the maximum and minimum points from a parabolic flight experiment as training, we find the KRR-HeITL model can obtain a MAPE of <5% on zero-gravity data. We conclude that the KRR-HeITL model performs well on interpolation of zero-gravity data but falls short when predicting points outside of the range it was trained on. This study validates that transfer learning can be used as an effective way to transfer physics-based parameters from on-ground to "in-space" experiments. The KRR-HeITL model could be a valuable tool for exploring other domain shifts in AM such as electron beam freeform fabrication, FFF, and DIW since they have been studied for their applicability in zero gravity [15,16,18], and the application of KRR-HeITL to these fields could further validate and enhance the model. Transfer learning's use in the development phase has the potential to accelerate material, mechanical, and chemical testing, especially since our means for zero-gravity experiments stay limited. We anticipate that this research will motivate researchers to use transfer learning in more in-space manufacturing applications.

Acknowledgment

The project is sponsored by Professor Hantang Qin's startup funds at the University of Wisconsin–Madison, NASA Space Technology Graduate Research Opportunities (NSTGRO 80NSSC2XK1188) and NASA Award No. 80MSFC23PA012. We sincerely thank the support of our sponsors.

Conflict of Interest

There are no conflicts of interest.

Data Availability Statement

The datasets generated and supporting the findings of this article are obtainable from the corresponding author upon reasonable request.

Nomenclature

k = Gaussian RBF kernel
E = set of data collected "on earth" via laboratory experiments
S = set of data collected "in space" via parabolic flight tests
M = number of S_r training data points
N = number of E data points
D = number of features
$\hat{w}$ = weight function
$\hat{W}$ = the diagonal matrix containing $\hat{w}$
a_E = model coefficients for normal kernel ridge regression on E data
y_i = target—printed line width
$\widehat{y_i}$ = model output—predicted line width
$\underline{\bar{y}_i}$ = mean of the target line widths
$\hat{\bar{y}}_i$ = mean of the predicted line widths
S_r = subset of S data to be used for training
S_t = subset of S data to be used for testing
$\hat{y}^\star$ = prediction of new data $x^\star$
$(x^\star, y^\star)$ = a new data point
γ = regularization parameter of squared loss function
η = kernel width hyperparameter of $\hat{w}^{a_E}$
θ = modified ridge regression model parameters
λ = regularization parameter of the modified ridge regression model
σ = kernel width hyperparameter of k
ϕ = feature map of the modified ridge regression model

References

[1] Hoffmann, M., and Elwany, A., 2023, "In-Space Additive Manufacturing: A Review," ASME J. Manuf. Sci. Eng., **145**(2), p. 020801.
[2] Prater, T., Werkheiser, N., Ledbetter, F., Timucin, D., Wheeler, K., and Snyder, M., 2018, "3D Printing in Zero G Technology Demonstration Mission: Complete Experimental Results and Summary of Related Material Modeling Efforts," Int. J. Adv. Manuf. Technol., **101**(1–4), pp. 391–417.
[3] "ESA Launches First Metal 3D Printer to ISS," European Space Agency. https://www.esa.int/Science_Exploration/Human_and_Robotic_Exploration/ESA_launches_first_metal_3D_printer_to_ISS, Accessed January 31, 2024.
[4] "Three Years of 3D Printing on the Space Station," The Center for the Advancement of Science in Space, Inc. (CASIS), https://www.issnationallab.org/three-years-of-3d-printing-on-the-space-station/, Accessed March 25, 2019.
[5] Haga, M., Maekawa, T., Kuwahara, K., Ohara, A., Kawasakl, K., Harada, T., Yoda, S., and Nakamura, T., 1995, "Effect of Electric Field on Marangoni Convection Under Microgravity," J. Japan Soc. Microgravity Appl., **12**(1), p. 19.
[6] Edwards, A. P. R., Osborne, B. P., Stoltzfus, J. M., Howes, T., and Steinberg, T. A., 2002, "Instabilities and Drop Formation in Cylindrical Liquid Jets in Reduced Gravity," Phys. Fluids, **14**(10), pp. 3432–3438.
[7] Osborne, B. P., and Steinberg, T. A., 2006, "An Experimental Investigation Into Liquid Jetting Modes and Break-Up Mechanisms Conducted in a New Reduced Gravity Facility," Microgravity Sci. Technol., **18**(3–4), pp. 57–61.
[8] Li, W., Lan, D., and Wang, Y., 2020, "Exploration of Direct-Ink-Write 3D Printing in Space: Droplet Dynamics and Patterns Formation in Microgravity," Microgravity Sci. Technol., **32**(5), pp. 935–940.
[9] Zocca, A., Lüchtenborg, J., Mühler, T., Wilbig, J., Mohr, G., Villatte, T., Léonard, F., et al., 2019, "Enabling the 3D Printing of Metal Components in μ-Gravity," Adv. Mater., **4**(10), p. 1900506.
[10] D'Angelo, O., Kuthe, F., Liu, S.-J., Wiedey, R., Bennett, J. M., Meisnar, M., Barnes, A., Kranz, W. T., Voigtmann, T., and Meyer, A., 2021, "A Gravity-Independent Powder-Based Additive Manufacturing Process Tailored for Space Applications," Addit. Manuf., **47**, p. 102349.
[11] Reitz, B., Lotz, C., Gerdes, N., Linke, S., Olsen, E., Pflieger, K., Sohrt, S., et al., 2021, "Additive Manufacturing Under Lunar Gravity and Microgravity," Microgravity Sci. Technol., **33**(2), pp. 1–12.
[12] Taminger, K. M. B., Harley, R. A., and Dicus, D. L., 2002, *Solid Freeform Fabrication: An Enabling Technology for Future Space Missions*, Metals and Thermal Structures Branch, NASA Langley Research Cente, Hampton, VA.
[13] Gu, H., and Li, L., 2019, "Computational Fluid Dynamic Simulation of Gravity and Pressure Effects in Laser Metal Deposition for Potential Additive Manufacturing in Space," Int. J. Heat Mass Transfer, **140**, pp. 51–65.

[14] Dou, R., Tang, W., Hu, K., and Wang, L., 2022, "Ceramic Paste for Space Stereolithography 3D Printing Technology in Microgravity Environment," J. Eur. Ceram. Soc., **42**(9), pp. 3968–3975.

[15] Hafley, R. A., Taminger, K. M. B., and Bird, R. K., 2007, *Electron Beam Freeform Fabrication in the Space*, NASA Langley Research Center, Hampton, VA.

[16] Zhang, J., Van Hooreweder, B., and Ferraris, E., 2022, "Fused Filament Fabrication on the Moon," J. Miner. Met. Mater. Soc., **74**(3), pp. 1111–1119.

[17] Kauzya, J.-B., Hayes, B., Hayes, A. C., Thompson, J. F., Bellerjeau, C., Evans, K., Osio-Norgaard, J., et al.et al., 2024, "Direct Ink Writing of Viscous Inks in Variable Gravity Regimes Using Parabolic Flights," Acta Astronaut., **219**, pp. 569–579.

[18] Qu, M., Meng, Z., Gao, T., He, J., and Li, D., 2023, "Exploration of Electrohydrodynamic Printing Potentially for In-Space Fabrication of Microscale Functional Structures: A Preliminary Study by an Anti-Gravity Configuration," Addit. Manuf., **61**, p. 103349.

[19] Lyu, H., Zhang, X., Liu, F., Huang, Y., Zhang, Z., Jiang, S., and Qin, H., 2019, "Fabrication of Micro-Scale Radiation Shielding Structures Using Tungsten Nanoink Through Electrohydrodynamic Inkjet Printing," J. Micromech. Microeng., **29**(11), p. 115004.

[20] Zeleny, J., 1917, "Instability of Electrified Liquid Surfaces," Am. Phys. Soc., **10**(1), p. 1.

[21] Taylor, G., "Disintegration of Water Drops in an Electric Field," Proc. R. Soc. London, Ser. A, **280**(1382), pp. 383–397.

[22] Mkhize, N., and Bhaskaran, H., 2021, "Electrohydrodynamic Jet Printing: Introductory Concepts and Considerations," Small Sci., **2**(2), p. 2100073.

[23] Han, Y., and Dong, J., 2018, "Electrohydrodynamic Printing for Advanced Micro/Nanomanufacturing: Current Progresses, Opportunities, and Challenges," ASME J. Micro Nano-Manuf., **6**(4), p. 040802.

[24] Jayasinghe, S. N., Qureshi, A. N., and Eagles, P. A. M., 2006, "Electrohydrodynamic Jet Processing: an Advanced Electric-Field-Driven Jetting Phenomenon for Processing Living Cells," Small, **2**(2), pp. 216–219.

[25] Altun, E., Ekren, N., Kuruca, S. E., and Gunduz, O., 2019, "Cell Studies on Electrohydrodynamic (EHD)-3D-Bioprinted Bacterial Cellulose \Polycaprolactone Scaffolds for Tissue Engineering," Mater. Lett., **234**, pp. 163–167.

[26] Khan, S., Hoi Doh, Y., Khan, A., Rahman, A., Choi, K. H., and Kim, D. S., 2011, "Direct Patterning and Electrospray Deposition Through EHD for Fabrication of Printed Thin Film Transistors," Curr. Appl. Phys., **11**(1), pp. S271–S279.

[27] Jang, Y., Kim, J., and Byun, D., 2013, "Invisible Metal-Grid Transparent Electrode Prepared by Electrohydrodynamic (EHD) Jet Printing," J. Phys. D: Appl. Phys., **46**(15), p. 155103.

[28] Huang, Y., Cao, Y., and Qin, H., 2022, "Electric Field Assisted Direct Writing and 3D Printing of Low-Melting Alloy," Adv. Eng., **24**(9), p. 2200091.

[29] Jiang, L., Li, W., Wolf, R., Marander, M., Kirscht, T., Liu, F., Jones, J. M., Hill, C., Jiang, S., and Qin, H., 2024, "High-Sensitivity Fully Printed Flexible BaTiO3-Based Capacitive Humidity Sensor for In-Space Manufacturing by Electrohydrodynamic Inkjet Printing," IEEE Sens. J., **24**(15), pp. 24659–24667.

[30] Ahmad, S., Rahman, K., Shakeel, M., Qasuria, T., Cheema, T., and Khan, A., 2021, "A Low-Cost Printed Humidity Sensor on Cellulose Substrate by EHD Printing," J. Mater. Res., **36**(18), pp. 3667–3678.

[31] Ahn, J.-H., Hong, H.-J., and Lee, C.-Y., 2021, "Temperature-Sensing Inks Using Electrohydrodynamic Inkjet Printing Technology," Materials, **14**(19), p. 5623.

[32] Li, B., Liang, W., and Ren, F., 2022, "Electrohydrodynamic (EHD) Inkjet Printing Flexible Pressure Sensors With a Multilayer Structure and Periodically Patterned Ag Nanoparticles," J. Mater. Sci.: Mater. Electron., **33**(11), pp. 18734–18750.

[33] Zhang, X., Chi, X., Li, Z., Yuan, Z., Yang, J., Zhu, L., and Zhang, F., 2020, "An Electrohydrodynamic (EHD) Printing Method With Nanosilver Ink for Flexible Electronics," Int. J. Mod. Phys. B, **34**(17), p. 2050154.

[34] Wang, H., Zhang, Y., Liu, Y., Chen, Z., Li, Y., Lia, X., and Xu, X., 2023, "High-Efficiency and High-Resolution Patterned Quantum Dot Light Emitting Diodes by Electrohydrodynamic Printing," Nanoscale Adv., **5**(4), pp. 1183–1189.

[35] Li, H., Duan, Y., Shao, Z., Zhang, G., Li, H., Huang, Y., and Yin, Z., 2020, "High-Resolution Pixelated Light Emitting Diodes Based on Electrohydrodynamic Printing and Coffee-Ring-Free Quantum Dot Film," Adv. Mater., **5**(10), p. 2000401.

[36] Jiang, L., Yu, L., Premaratne, P., Zhang, Z., and Qin, H., 2021, "CFD-Based Numerical Modeling to Predict the Dimensions of Printed Droplets in Electrohydrodynamic Inkjet Printing," J. Manuf. Process., **66**, pp. 125–132.

[37] Singh, S. K., Rai, N., and Subramanian, A., 2023, "Machine Learning-Informed Predictive Design and Analysis of Electrohydrodynamic Printing Systems," Adv. Eng., **25**(19), p. 2300740.

[38] Qin, J., Hu, F., Liu, Y., Witherell, P., Wang, C. C. L., Rosen, D. W., Simpson, T. W., Lu, Y., and Tang, Q., 2022, "Research and Application of Machine Learning for Additive Manufacturing," Addit. Manuf., **52**, p. 102691.

[39] Wang, C., Tan, X. P., Tor, S. B., and Lim, C. S., 2020, "Machine Learning in Additive Manufacturing: State-of-the-Art and Perspectives," Addit. Manuf., **36**, p. 101538.

[40] Piovarči, M., Foshey, M., Xu, J., Erps, T., Babaei, V., Didyk, P., Rusinkiewicz, S., Matusik, W., and Bickel, B., 2022, "Closed-Loop Control of Direct Ink Writing Via Reinforcement Learning," ACM Trans. Graphics, **41**(4), pp. 1–10.

[41] Zhang, X., Lies, B., Lyu, H., and Qin, H., 2019, "IN-Situ Monitoring of Electrohydrodynamic Inkjet Printing Via Scalar Diffraction for Printed Droplets," J. Manuf. Syst., **53**, pp. 1–10.

[42] Jiang, L., Premaratne, P., Huang, Y., Zhang, Z., and Qin, H., 2021, "Modeling and Experimental Validation of Droplet Generation in Electrohydrodynamic Inkjet Printing for Prediction of Printing Quality," Proceedings of the ASME 2021 16th International Manufacturing Science and Engineering Conference, Virtual, June 21–25.

[43] Lu, L., Hou, J., Yuan, S., Yao, X., Li, Y., and Zhu, J., 2023, "Deep Learning-Assisted Real-Time Defect Detection and Closed-Loop Adjustment for Additive Manufacturing of Continuous Fiber-Reinforced Polymer Composites," Rob. Comput. Integr. Manuf., **79**, p. 102431.

[44] Lies, B. T., Cai, Y., Spahr, E., Lin, K., and Qin, H., 2018, "Machine Vision Assisted Micro-Filament Detection for Real-Time Monitoring of Electrohydrodynamic Inkjet Printing," Procedia Manuf., **26**, pp. 29–39.

[45] Singh, S. K., and Sarma, S., 2022, "Taylor Cone Height as a Tool to Understand Properties of Electrospun PVDF Nanofibers," J. Electrostat., **120**, p. 103770.

[46] Mieszczanek, P., Robinson, T. M., Dalton, P. D., and Hutmacher, D. W., 2021, "Convergence of Machine Vision and Melt Electrowriting," Adv. Mater., **33**(29), p. 2100519.

[47] Iman, M., Arabnia, H., and Rasheed, K., 2023, "A Review of Deep Transfer Learning and Recent Advancements," Technologies, **11**(2), p. 40.

[48] Zhuang, F., Qi, Z., Duan, K., Xi, D., Zhu, Y., and Zhu, H., 2019, "A Comprehensive Survey on Transfer Learning," Proc. IEEE, **109**(1), pp. 43–76.

[49] Pan, S., and Yang, Q., "A Survey on Transfer Learning," IEEE Trans. Knowl. Data Eng., **22**(10), pp. 1345–1359.

[50] Sun, J., Jing, L., Zhan, N., Huang, D., and Liang, Y. C., 2020, "Electrohydrodynamic Printing Process Monitoring for Diverse Microstructure Bioscaffold Fabrication," ICBET '20: Proceedings of the 2020 10th International Conference on Biomedical Engineering and Technology, Tokyo, Japan, Sept. 15–18, pp. 305–310.

[51] Friedjungová, M., and Jiřina, M., 2017, "Asymmetric Heterogeneous Transfer Learning: A Survey," Proceedings of the Sixth International Conference on Data Science, Technology and Applications DATA, Vol. 1, Madrid, Spain, July 24–26.

[52] Bamne, B., Shrivastava, N., Parashar, L., and Singh, U., 2020, "Transfer Learning-Based Object Detection by Using Convolutional Neural Networks," 2020 International Conference on Electronics and Sustainable Communication Systems (ICESC), Coimbatore, India, July 2–4.

[53] Cheng, L., Wang, K., and Tsung, F., 2020, "A Hybrid Transfer Learning Framework for In-Plane Freeform Shape Accuracy Control in Additive Manufacturing," IISE Trans., **53**(3), pp. 298–312.

[54] Aboutaleb, A. M., Bian, L., Elwany, A., Shamsaei, N., Thompson, S. M., and Tapia, G., 2016, "Accelerated Process Optimization for Laser-Based Additive Manufacturing by Leveraging Similar Prior Studies," IISE Trans., **49**(1), pp. 31–44.

[55] Zhang, H., Choi, J. P., Moon, S. K., and Ngo, T. H., 2021, "A Knowledge Transfer Framework to Support Rapid Process Modeling in Aerosol Jet Printing," Adv. Eng. Inform., **48**, p. 101264.

[56] Waisberg, E., Ong, J., Kamran, S. A., Paladugu, P., Zaman, N., Lee, A. G., and Tavakkoli, A., 2023, "Transfer Learning as an AI-Based Solution to Address Limited Datasets in Space Medicine," Life Sci. Space Res., **36**, pp. 36–38.

[57] Ogundipe, C., and Ellery, A., 2024, "Adaptive Solution to Transfer Learning of Neural Network Controllers From Earth to Space Environments," Expert Syst., p. e13549.

[58] He, J.-H., 2020, "On the Height of Taylor Cone in Electrospinning," Results Phys., **17**, p. 103096.

[59] Garcke, J., and Vanck, T., "Importance Weighted Inductive TransferLearning for Regression," 2014, *Machine Learning and Knowledge Discovery in Databases*, Springer Cham, Nancy, France.

[60] Sukhija, S., and Krishnan, N. C., 2019, "Supervised Heterogeneous Feature Transfer Via Random Forests," Artif. Intell., **268**, pp. 30–53.

[61] Shi, X., Liu, Q., Fan, W., Yu, P. S., and Zhu, R., 2010, "Ransfer Learning on Heterogenous Feature Spaces via Spectral Transformatio," 2010 IEEE International Conference on Data Mining, Sydney, Australia, Dec. 13–17.

[62] Li, S., Cai, T. T., and Li, H., 2022, "Transfer Learning for High-Dimensional Linear Regression: Prediction, Estimation and Minimax Optimality," J. R. Stat. Soc. Ser. B, **84**(1), pp. 149–173.

[63] Gosain, A., and Sardana, S., 2017, "Handling Class Imbalance Problem Using Oversampling Techniques: A Review," International Conference on Advances in Computing, Communications and Informatics (ICACCI), Udupi, India, Sept. 21–24.

[64] Krawczyk, B., 2016, "Learning From Imbalanced Data: Open Challenges and Future Directions," Prog. Artif. Intell., **5**(4), pp. 221–232.

[65] Hu, M., and Li, J., 2019, "Exploring Bias in GAN-Based Data Augmentation for Small Samples," arXiv.org.

[66] Matchev, K. T., Roman, A., and Shyamsundar, P., 2022, "Uncertainties Associated With GAN-Generated Datasets in High Energy Physics," SciPost Phys., **12**(3), p. 104.